Conference Paper, Published Version

Klar, M.; Jehle, M.; Jähne, Bernd; Detert, M.; Jirka, Gerhard H.; Köhler, Hans-Jürgen; Wenka, Thomas

Analysis of Subsurface Gravel Layer Flow caused by Turbulent Open Channel Flow using 3-D PTV and Pressure Sensor Techniques (Untersuchung der Interaktion von Haupt- und Interstitialströmung mit Hilfe von 3-D PTV und piezoresistiven Drucksensoren)

9 Analysis of Subsurface Gravel Layer Flow caused by Turbulent Open Channel Flow using 3-D PTV and Pressure Sensor Techniques

Untersuchung der Interaktion von Haupt- und Interstitialströmung mit Hilfe von 3-D PTV und piezoresistiven Drucksensoren

M. Klar, M. Jehle, B. Jähne

Interdisziplinäres Zentrum für Wissenschaftliches Rechnen (IWR), Universität Heidelberg
Interdisciplinary Center for Scientific Computing (IWR), University of Heidelberg, Germany

M. Detert, G.H. Jirka

Institut für Hydromechanik (IfH), Universität Karlsruhe
Institute for Hydromechanics (IfH), University of Karlsruhe, Germany

H.-J. Köhler, T. Wenka

Bundesanstalt für Wasserbau (BAW), Karlsruhe
Federal Waterways Engineering and Research Institute (BAW), Karlsruhe, Germany

ABSTRACT: This paper contains results from an experimental study on the fields of river bed stability. A contribution to a synoptic view of velocity- and pressure-fields above and within a gravel bed shall be given. Combined measurements are carried out with miniature temporally high resolution pressure sensors and with optical flow measurement techniques. 2-D and 3-D flow velocities are obtained by digital image sequence analysis (3-D Particle-Tracking Velocimetry, 2-D Optical Flow Techniques). The novel measurement techniques are presented and exemplary data sets are analysed in detail. The results shall contribute to an improved understanding of the processes of erosion and sedimentation, as well as mass exchange processes. The long-term goal of this project is to improve the design criteria for bed stability in waterways.

KURZFASSUNG: In diesem Aufsatz werden Ergebnisse einer experimentellen Untersuchung zur Sohlstabilität zusammengestellt. Ziel der Untersuchung ist eine synoptische Erfassung der Strömungs- und Druckfelder oberhalb und im Porenraum einer Kiessohle durch simultane, zeitlich hochaufgelöste Messungen von Druck und Geschwindigkeit. Dazu werden miniaturisierte Piezo-Drucksensoren zur Druckmessung sowie optische 2D- und 3D-Techniken zur Strömungsmessung eingesetzt. Die Auswertung der Geschwindigkeitsmessungen erfolgt durch digitale Bildsequenzanalyse (3-D Particle-Tracking Velocimetry, 2-D Optischer Fluss). Die neu entwickel-ten Messtechniken sowie exemplarische Messergebnisse werden vorgestellt. Die Ergebnisse sollen zu einem besseren Verständnis von Erosions- und Sedimentationsprozessen sowie von Austauschprozessen (Masse, Impuls) zwischen Oberflächen- und Porenströmung beitragen. Das langfristige Ziel dieses Projekts ist die Verbesserung der ingenieurtechnischen Bemessung von Sohlschutzmassnahmen.

9.1 Introduction

The challenges of hydraulic engineering in river and waterways depend essentially on the prediction of the morphodynamical development of the river bed. The efficiency of regulation works or hydraulic constructions such as groynes, weirs or mounted embankments are strongly influenced by the stability of the river bed and the artificial geotechnical armoring layer, respectively. For example, the Iffezheim barrage at the Rhine-river near Karlsruhe needs about 200.000 m³ of gravel additionally per year to avoid erosion in the downstream river bed.

Over the last 100 years much research work has been done to gain insight into the theoretical background of river bed stability. /Shields 1936/ developed a non-dimensional diagram to describe the transition from a stable to a moving bed, which can be seen as the 'classical' approach in river bed stability. Diverse formulae have been developed to improve this approach, e.g. /Meyer-Peter & Müller 1949/; /Bonnefille 1963/; /Grass 1970/; /Wilcock 1993/. However, up to now no satisfactory, physically founded formula has been established to answer definitely the question of river bed stability. The understanding of the individual processes, the functional chain of cause and effect is not developed far enough to predict destabilization. Hence, the success of a hydraulic construction cannot be guaranteed satisfactorily.

9.2 Background

For a more detailed consideration of stability problems the analysis of the influence of fluctuating forces is important, e.g. /Dittrich et al. 1999/; /Zanke 2001/. Fluctuating forces might be caused by turbulence of open-channel flow including the occurrence of coherent structures as well as the involvement of the whole hydrodynamic system which consists of free surface flow, combined with the subsurface gravel layer and eventually the groundwater flow.

The discovery of the so-called bursting phenomenon in turbulent flows by /Kline 1967/ generated a new interest in studying the structures of boundary layer turbulence. As it is described by /Grass 1971/, fluid near the bottom is thrown upwards during an ejection phase, during a sweep phase fluid is pumped towards the bottom. Burst-cycles occur over both smooth and rough surfaces. They have a strong impact on pressure peaks on the bottom which might cause the erosion of single grains /Drake 1988/; /Gyr et al. 1996/. /Emmerling 1973/ noticed instantaneous pressure peaks max(p) as high as six times the medium pressure fluctuations rms(p). /Raudkivi 1982/ as well as /Dittrich et al. 1999/ correlate rms(p) to shear stress τ_0 as

$$rms(p) = C\,\tau_0 \qquad\qquad (9\text{-}1)$$

with C varying from 0.5 to 5.0, with an average of 3.0. Referring to /Emmerling 1973/ max(p) must be taken into consideration up to 18 τ_0!

Recent developments in measuring techniques allow to get a more enclosing view of the processes that lead to an instable bed /Detert et al. 2004; Klar et al. 2004/. The use of optical flow measurement techniques combined with piezometric micro pressure sensors (MPS) above as well as within a gravel layer are an excellent tool to get a more synoptic view of the related processes.

9.3 Experimental Setup

9.3.1 Flume

The experimental system has been implemented in an open channel flume located at the Federal Waterways Engineering and Research Institute (Bundesanstalt für Wasserbau, BAW). The flume is L = 40 m long and B = 0.9 m wide. The maximum flow rate is Q_{max} = 0.275 m³/s (Figure 9.1)

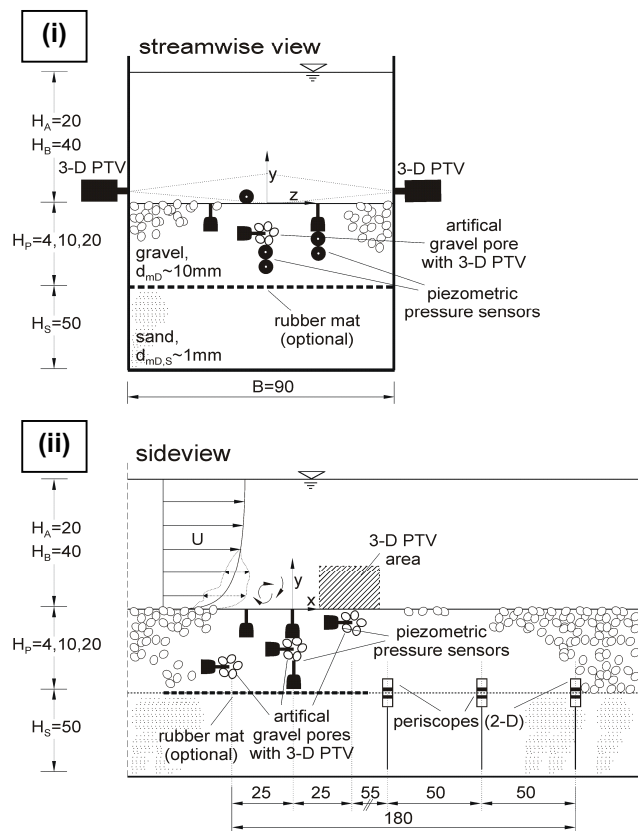*Figure 9.1   Sketch of experimental setup, dimensions [cm], not to scale, (i) streamwise view with the positions of the cameras for the free surface 3-D PTV and the piezometric pressure sensors, (ii) side view, where also the positions of the artificial gravel pores and the periscopes can be seen.*

A sand layer of height H_S = 0.5 m covered by a porous gravel layer of height H_P = 0.04 to 0.20 m is

placed in the flume over an effective length of $L = 30$ m, optionally with and without hydraulic contact to the sand layer. This is achieved by omitting or inserting a rubber mat at the interface. The measuring-area is located in the middle of the flume at 15 m, hence influences of inlet and outlet are supposed to be negligible. The medium grain diameter of the gravel is $d_{mD} = {\sim}10$ mm, with a degree of non-uniformity $C_c = d_{60}/d_{10} = 1.25$. The pore number can be calculated to $\varepsilon = 62.4$ % (loose density: 1.538 g/cm³, grain density: 2.464 g/cm³). The mean grain diameter of the uniform sand is about $d_{mD,S} = {\sim}1$ mm. The measuring program is defined for water depth of $H_A/d_{mD} = 20$ and $H_B/d_{mD} = 40$, as it can be seen in Table 9.1.

series	H_p/d_{mD}	stability criteria τ_0/τ_{0c}					
		0.0	0.1	0.2	0.4	0.6	>0.6
series 1: gravel/sand	20	-	-	-	-	-	-
	10	$W_{A,B}$	$W_{A,B}$	-	$H_{A,B}$	H_A	-
	4	$W_{A,B}$	$W_{A,B}$	$H_{A,B}$	$H_{A,B}$	H_A	H_A
series 2: gravel	20	$W_{A,B}$	$W_{A,B}$	$H_{A,B}$	$H_{A,B}$	-	-
	10	$W_{A,B}$	$W_{A,B}$	$H_{A,B}$	$W_{A,B}$	H_A	H_A
	4	$W_{A,B}$	$H_{A,B}$	$H_{A,B}$	$H_{A,B}$	H_A	H_A
series 3: glass spheres	20	-	-	-	-	-	-
	10	-	-	-	-	-	-
	4	$H_{A,B,C}$	$H_{A,B,C}$	$H_{B,C}$	H_A	-	-
explanation:	$H_{A,B,C}$	water depth $H_{A,B,C}/d_{mD} = 20, 40, 10$					
	$W_{A,B}$	additional gauging incl. wave generator					
	H_p	heigth of porous granular filter					
	d_{mD}	mean gravel diameter					

Table 9.1   Measuring program, with increasing shear stress τ_0/τ_{0c}, $\tau_{0c} = 8.8$ Pa (Shields).

Variation in discharge and water depth provides flow conditions up to low mobility transport conditions based on /Shields 1936/ parameter, τ^*. Supplementary gauges will be made with glass spheres, having a $d_{mD} = 10$ mm.

Figure 9.2   Photo of the Wave Generator in the BAW flume.

Long waves are generated artificially by a wave generator located 9.25 m downstream from the measuring-area. Thus, the influence of an oscillating water level can be studied. Figure 9.2 shows a photograph of the wave generator.

The flow rate is measured by a magnetic inductive flowmeter, the water level is detected by an external ultrasonic probe with hydraulic contact to the flume. Steady flow conditions for each measurement are provided by controlling the gate valve at the inlet and the movable weir at the outlet automatically.

At the measurement area, optical access to the flume is given by plexiglass windows inserted into the channel walls over a length of 4 m, where the experimental instrumentation is installed (Figure 9.1). In particular, the setup consists of the following parts:

- a stereo camera setup for the investigation of the free surface flow above the gravel layer,

- three endoscopic stereo setups to record the flow fields inside the gravel layer with specially prepared artificial gravel pores,

- three rigid endoscopes inserted from below the channel to observe the sand-gravel-boundary,

- up to ten pressure sensors at arbitrary locations within the gravel layer (three of the sensors are attached to the artificial gravel pores used for the flow measurement).

The data acquisition is carried out simultaneously for all the systems, which are described in more detail in the following sections.

To gain additional insight into the velocity in streamwise direction in the free surface flow an 1D-Acoustic Doppler Profiler (ADCP) was used. The ADCP was installed 3.0 m downstream the measurement area and did not operate simultaneously to the other measuring probes.

9.3.2   3-D PTV

9.3.2.1   Free Surface Flow

In order to acquire stereoscopic image sequences of the free surface flow, two CCD-cameras (Pulnix TM 6701 AN) are mounted on the left and right side of the flume, viewing the center of the channel in upstream direction through the glass windows (Figure 9.3). The optical axes of the two cameras enclose an angle of about 90 degrees, maximizing the size of the stereo volume (about 5 cm in all directions), which is viewed by both cameras. Two glass prisms filled with water are attached to the channel side windows to make the optical axes of the cameras perpendicular to the air-glass interface. In this way, refraction effects of the optical rays passing the multimedia interfaces are minimized. Three halogen lamps are used to illuminate the stereo volume from above the water surface. Visualization of the flow is

provided by small air bubbles suspended in the water.

To enable particle tracking at large flow velocities, the frame rate of the cameras must be high enough to keep the displacements of the particles between successive images within certain limits. For standard video capturing, the Pulnix TM 6701 AN delivers images of 640 by 480 pixels at a frame rate of 60 Hz. However, the camera also offers a partial scan mode, reducing the image size to 640 by 200 pixels, but increasing the frame rate up to 125 Hz. This mode has been used for the measurements.

The acquired image sequences have to be stored in the computer memory before they are written to a hard-disk. Thus, the maximum duration of one stereo image sequence of the free surface flow is about $\Delta t = 20$ s, limited by the PC memory.

Figure 9.4   Endoscope stereo setup. For velocity measurements in the gravel layer, this stereo rig is attached to the artificial pores, viewing the pore volume inside.
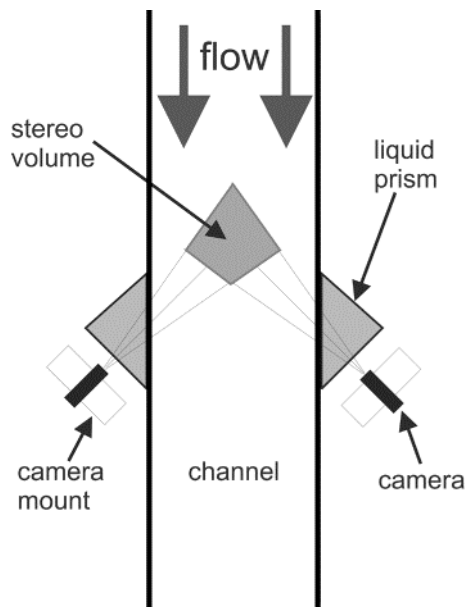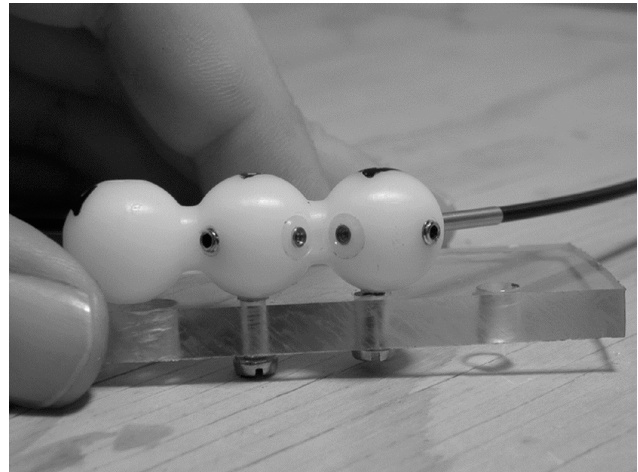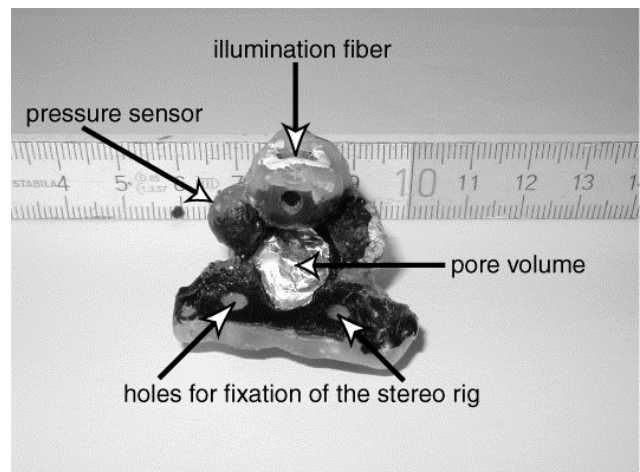

Figure 9.3   Top view of the stereo camera setup for 3-D PTV above the gravel layer. The cameras view the channel in up-stream direction through water-filled glass prisms attached to the channel side walls.

Figure 9.5   Artificial gravel pore.

9.3.2.2   Pore Flow

Flow measurements inside three single pores of the gravel layer are carried out using three miniaturized endoscopic stereo setups. The basic principle of these setups is the same as for the free surface flow, namely to acquire stereoscopic image sequences of the flow field inside the pore volume by viewing it from two different directions. Two flexible fiber-optic endoscopes of 2.4 mm diameter are attached to an adapted artificial gravel pore made of grains fixed to each other (Figures 9.4 and 9.5).

Illumination of the pore volume is provided by an optical fiber-bundle guiding the light from a halogen cold light source into the pore. The purpose of the artificial pore is to hold the endoscopes and the illumination fiber at a fixed relative position and to keep surrounding grains in the gravel layer from blocking the endoscope view. To perform flow measurements, the three artificial pores are embedded in the gravel layer at different positions (Figure 9.6). A solution of tracer particles is added to the flow upstream of the pores, and particle image sequences of the two different endoscope views are recorded simultaneously.

The size of the observation volume inside the pores is about 5 mm in all directions. Since the tracer particles cover this small volume very rapidly, the cameras must have even higher frame rates than in the case of the free surface flow. Hence, two of the three artificial pores are equipped with high-speed Megapixel-CMOS-cameras (Photonfocus MV-

D1024). These cameras allow to read out only a region of interest on the sensor, which has been set to a size of 184 by 184 pixels. Zoom optics are used to fit the endoscope image to this image size on the sensor.
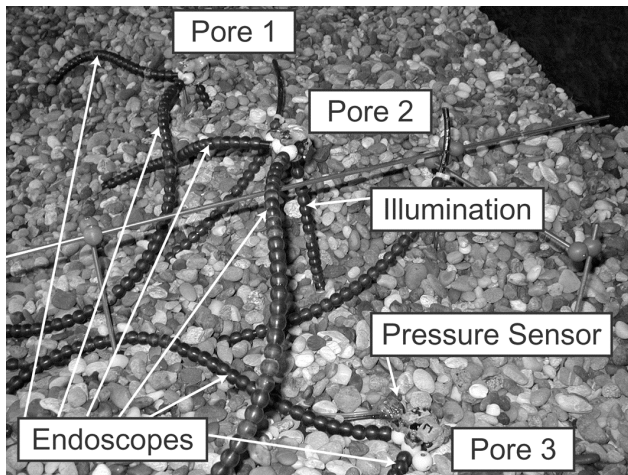

Figure 9.6   Installation of the three artificial pores in the gravel layer.

By decreasing the image resolution in this way, a maximum frame rate of 400 Hz can be achieved. The third endoscope setup is working with standard CCD-cameras running at 50 Hz. This setup can only be used in the lowermost position within the gravel layer, where the flow velocities are expected to be lowest.

The image data of all three setups are written to RAID hard-disk arrays in real-time during the acquisition. Thus, the duration of the sequences is only limited by the RAID capacity. For a single measurement, a sequence duration of 60 s has been chosen.

9.3.3   Sand Movement

Sediment movement is detected by three rigid endoscopes (Figures 9.7 and 9.8), inserted into the flume from below. The effects of sediment motion are expected to occur at the gravel-sand interface. The goal is to record a sequence of two-dimensional images, which can be analyzed by Optical Flow Techniques as described below. Thus, the requirements of the endoscopic setup are:

- Observation of the process of sediment motion should be as contact-free as possible.

- A large observation area is needed.

- A working distance of a defined distance should be kept.

- Sufficient and homogeneous illumination should be provided.

- The setup has to be reliable in the rough environment of the flume.

In order to meet these demands, special protection heads have been designed (Figure 9.7). With an aperture angle of 90 degrees and a viewing distance of approximately 7 mm, a circular area of about 12 mm in diameter can be observed.

Figure 9.7   Rigid endoscope for subsoil observation. The endoscope is inserted into a protection tube containing the illumination fibers, which can be seen at the corners of the glass window.

Figure 9.8   Rigid endoscopes inserted into the flume from below to observe motion of sand grains.

Standard CCD-cameras (SONY XC-73CE) have been used for image acquisition. Image sequences are acquired at a resolution of 512 by 512 pixels and

a frame rate of 25 Hz. Thus a data thruput of approximately 20 MB/s is achieved for all three endoscopes. Image sequences can be written to a RAID system in real-time during the acquisition.

9.3.4 Micro Pressure Sensors (MPS)

The micro pressure sensors (MPS) were manufactured in a cooperation of /Aktiv Sensor GmbH, Berlin/ and the Institute for Hydromechanics (IfH). The principle of these in-situ micro-pressure sensors is based on the 'piezoresistive' effect. The initial point is an element of silicium, with implanted resistances in its bending panel. Figure 9.9 shows a photograph of the encapsulated head of the pressure pickup and its flexible tube for pressure equalisation.
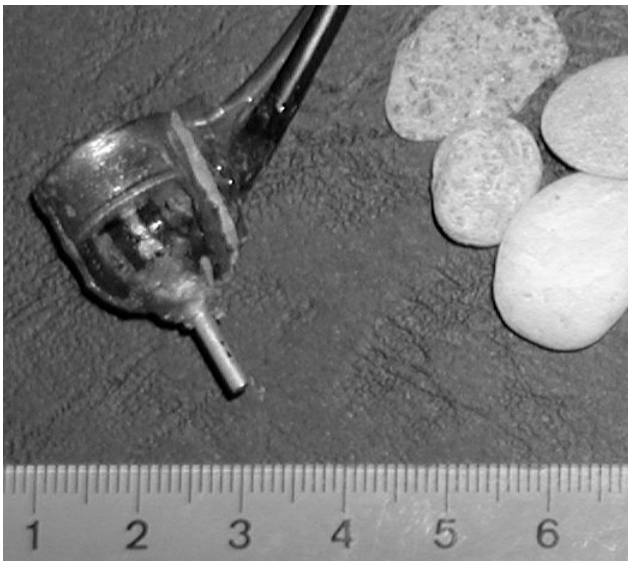
Figure 9.9   Head of micro pressure sensor outside the flume and above gravel d_{mD} = 10 mm

The differential pressure is measured in reference to atmospheric pressure, with compensation of temperature. The sensors are encapsulated with slowly hardening epoxy resin and sealed up with clear varnish to make them water resistant.The maximal dimensions of the sensors are 2×1.2×1.2 cm³, with a shape similar to a bigger gravel grain. Due to signal conditioning by the purpose-built amplifier the guaranteed maximum measurable frequencies are 100 Hz. Hence, measurements of pressure fluctuations up to the estimated Kolmogorov-scale-frequency of 50 Hz after /Nezu and Nakagawa 1993/ is possible. To avoid aliasing effects, the measurements are performed at a rate of 500 Hz.

The encapsulated sensors were calibrated by /Aktiv Sensor GmbH/ to 0 to 10 V according to 0 to 6 kPa at pressure of 3 and 6 kPa with a tolerance in accuracy of less than 1.0% full scale. The absolute range of the pressure sensors is 0 to 6 kPa. The accuracy due to the AD-card is limited to 0.15

mmWC. However, due to the dithering effect the accuracy was improved to > 0.003 mmWC for f < 20 Hz and > 0.012 mmWC for f > 20 Hz respectively. Figure 9.10 shows an example of a recorded signal.
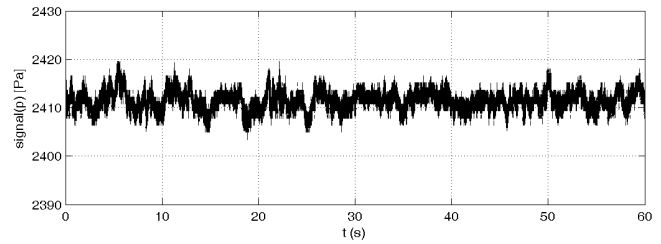
Figure 9.10   Pressure signal [Pa] at y/d_{mD} = -1.5 within the gravel layer, τ_0/τ_{0c} = 0.1, τ_{0c} = 8.8 Pa (Shields), H_A/d_{mD} = 21, H_P/d_{mD} = 20, no hydraulic contact between gravel and sand layer

Pressure sensors were located at vertical positions of y/d_{mD} = 1.0 (above), 0.0 (at top) and at various positions within the gravel layer. On each of the three artificial gravel pores a sensor was adapted to gain simultaneously insight in pressure and velocity. Simultaneous measurements were performed by up to ten pressure sensors over two minutes. The sensors were locally fixed on a grid as shown in Figure 9.11.

Figure 9.11   Photo of sensor above the gravel layer at y/d_{mD} = 1.0

After a few months in use the sensors showed an offset of up to 1 V corresponding to 0 Pa. Tests showed that the calibrating factor of 1.67 V/kPa stayed the same. Thus, on one hand the maximum detectable static pressure is reduced to 90 %, on the other hand the measurement of fluctuations is not affected. To gain the correct static pressure the sensors were calibrated before every measurement series by comparing the measured signal with the water level detected by an ultrasonic probe.

Furthermore, tests under flume-conditions at the BAW showed that an extraneous high frequency noise was disturbing the amplified signal, as it can be seen in Figure 9.12. Comparing measurements in flumes at the IfH did not show these noise effects. Even after a systematic search the cause could not be identified exactly. We suppose that the noise comes from a hospital ~300 m away from the flume (radio waves from magnetic resonance tomography or other medical instruments).
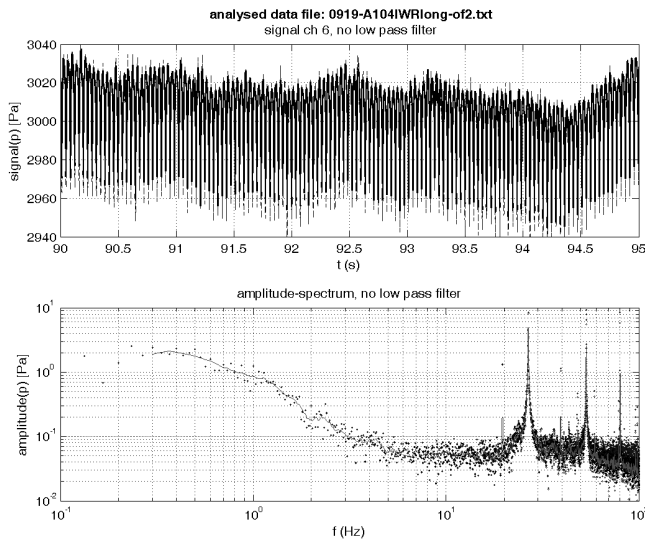

Figure 9.12   Example signal [Pa] and amplitude-spectrum [Pa] without low-pass filtering, τ_0/τ_{0c} = 0.4, H_A/d_{mD} = 20, H_P/d_{mD} = 10, hydraulic contact between gravel and sand layer

To suppress this noise, a low-pass filter with RC = 0.33 ms was used. Thus, the filter leads to damping of signals e.g. with 50 Hz to 99.5 % and signals with 10 kHz to 4.8 % which is acceptable for the provided flow conditions. The effect of the filter on the signal is shown in Figure 9.13.

Some of the pressure sensors lead to difting signals as shown in Figure 9.14. Figure 9.15 shows a signal measured simultaneously under the same flow conditions without any drift. Thus, the provided flume conditions must have been constant. Gauged drifting signals as in Figure 9.14 were omitted.
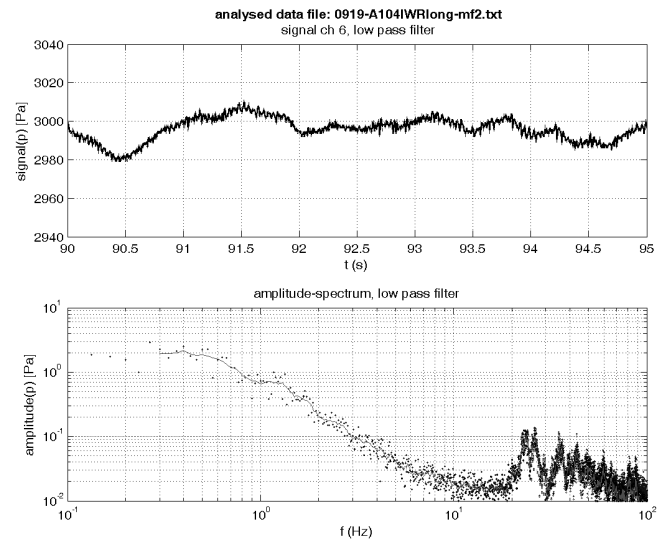

Figure 9.13   Example signal [Pa] and amplitude-spectrum [Pa] with low-pass filtering, the same flow conditions as in Figure 9.12, but not measured simultaneously
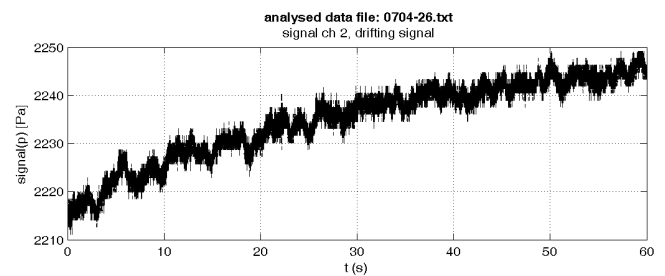

Figure 9.14   Signal [Pa] with drift, τ_0/τ_{0c} = 0.1, H_A/d_{mD} = 20, H_P/d_{mD} = 20
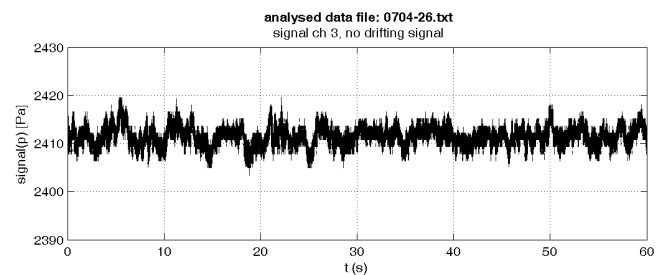

Figure 9.15   Signal [Pa] without drift, measured simultaneously with the signal in Figure 9.14

9.4　Preliminary Results

In this section, some results obtained with the presented setup are discussed. In addition to the development of the experimental apparatus and the performance and analysis of measurements, a significant part of the work carried out within this project is also the development of image processing algorithms, especially for 3-D PTV. Driven by the special demands of the endoscopic imaging, extensive improvements and adaptations of the existing software have to be implemented in order to guarantee an optimal performance of the algorithms. This work is still in progress. Therefore the results shown here have to be considered as preliminary examples. A comprehensive analysis of all results is subject of future work.

In the discussion, the following (right-handed) coordinate system (x,y,z) will be used (with corresponding velocity components (u,v,w)):

x,u:　coordinate in streamwise direction, increasing in flow direction,

y,v:　vertical coordinate, origin at the gravel-water-interface, defined at 25% of d_{mD} below the upper edge of the gravel grains,

z,w:　spanwise coordinate, origin at the centerline of the flume.

9.4.1　3-D PTV

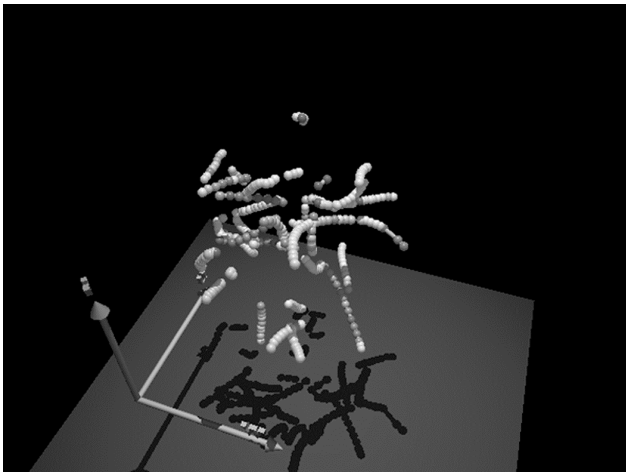#### 9.4.1.1　Pore Flow: 3-D Visualization

Figure 9.16　3-D visualization of the particle trajectories inside the pore volume.

Figure 9.16 shows a 3-D visualization of a reconstructed flow field. The Lagrangian particle trajectories within a time interval of 0.5 s can be seen in the image. The trajectories reveal that the flow field inside the pore is really three-dimensional, which underlines the need for a three-dimensional measurement technique.

9.4.1.2　Pore Flow: Velocity Time Series

In this experiment, two of the artificial pores have been positioned at the uppermost position in the gravel layer at y = -2 cm, i.e. 2 cm below the interface towards the free surface flow. The separation between the pores in x-direction was 25 cm as it can be seen in Figure 9.1. The pore volume of one of the pores was in direct contact with the free surface flow via an opening in vertical direction (this pore is referred to as "open" pore in the following). At the other pore, this opening was covered by a single grain, so there was no direct contact with the free surface flow in vertical direction ("closed" pore in the following). An experiment has been carried out with a flow discharge of Q = 0.056 m^3/s and a water depth of H_A/d_{mD} = 20. These values correspond to a mean velocity in the free surface flow of about 0.3 m/s and 10 % of the critical shear stress for (gravel-)bed destabilization. Figures 9.17 and 9.18 show the first 30 s of the time series of the streamwise (u) and vertical (v) velocities inside the two pores. The time series have been calculated by spatial averaging of all velocity vectors inside the pore volume. The plots show the damping effect of the pebble covering the "closed" pore: the flow velocities inside this pore are significantly lower than in the "open" pore, in spite of the fact that both pores are located in the same vertical position at the gravel-water interface. The velocity fluctuations in the "closed" pore are also dampened: the standard deviations in the "closed" pore are approximately 50 % smaller than in the "open" pore.
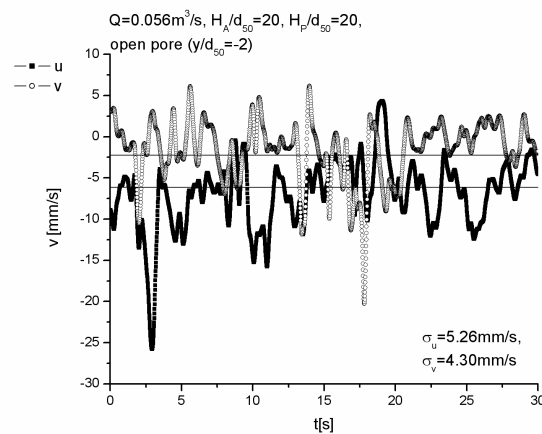

Figure 9.17　Time series of streamwise (u) and vertical (v) velocity in the "open" pore. The horizontal lines indicate the mean velocities.
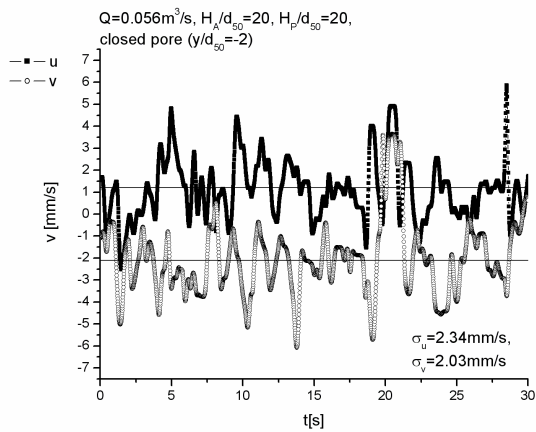
Figure 9.18   Time series of streamwise (u) and vertical (v) velocity in the "closed" pore. The horizontal lines indicate the mean velocities. Note the change of scale in the ordinate as compared to Figure 9.17.

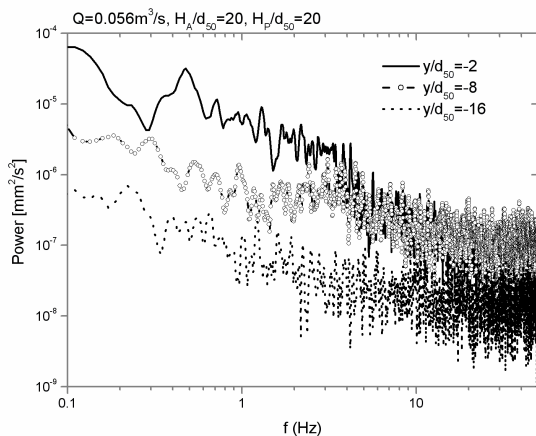### 9.4.1.3   Pore Flow: Power Spectra of Fluctuations

Figure 9.19   Power spectra of velocity data obtained from different vertical positions in the gravel layer. The damping effect of the gravel layer is evident.

In a second experiment, one of the artificial pores has been put in different vertical positions sequentially: y/d_{mD} = -2, -8 and -16. For each position, an image sequence has been acquired under the same flow conditions as in the experiment in section 9.4.1.1. Time series of the absolute value of the 3-D velocity have been calculated, again by spatial averaging of all the vectors inside the pore. Figure 9.19 shows the power spectra of the three velocity time series. The spectra show that the significant frequencies are in the range of 1 to 5 Hz. Further, at y/d_{mD} = -16, the amplitudes are roughly two orders of magnitude smaller than at y/d_{mD} = -2. Fluctuations in the pore flow are dampened with increasing depth in the gravel layer.

9.4.1.4   Free Surface Flow

3-D PTV results for the free surface flow are not available yet. However, in this section some results of a 2-D analysis are shown. Images of the left camera of the stereo setup have been evaluated. Figures 9.20a - 9.20e show a series of images, taken from a sequence which has been acquired in an experiment with a large surface wave (peak-to-peak amplitude 125 mm, period 2 s, water level 40 cm, height of gravel layer 4 cm). The images show a section of about 5 cm by 5 cm straight above the gravel layer, which is at the bottom of the images.

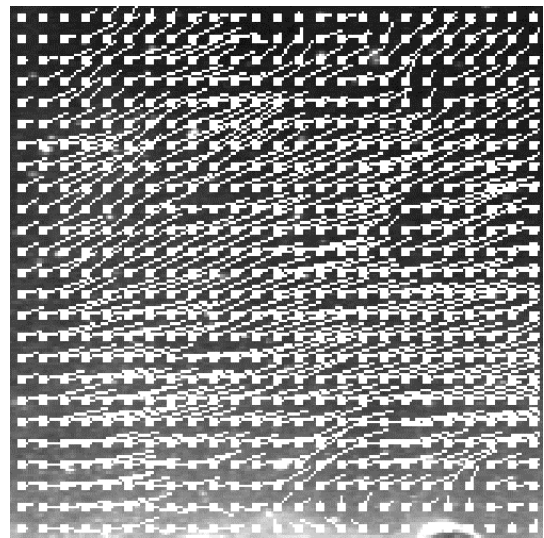*Figure 9.20a   Instantaneous flow field above the gravel layer, induced by a surface wave. Volume ~5x5x5 [cm³]. Mean flow is from left to right. Maximum downstream velocity, t = 0 s.*
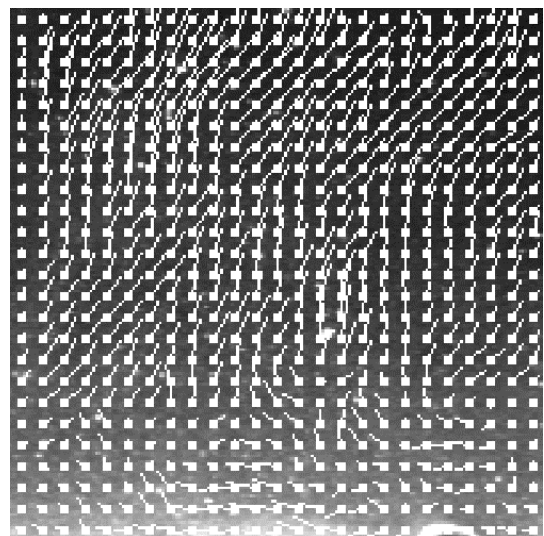

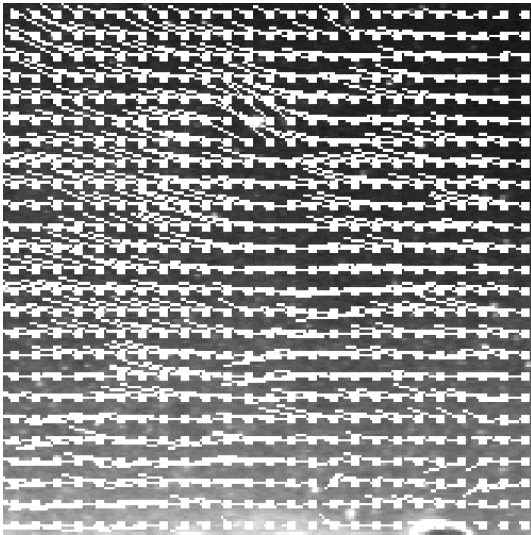*Figure 9.20b   Minimum streamwise velocity, t = 0.16 s.*

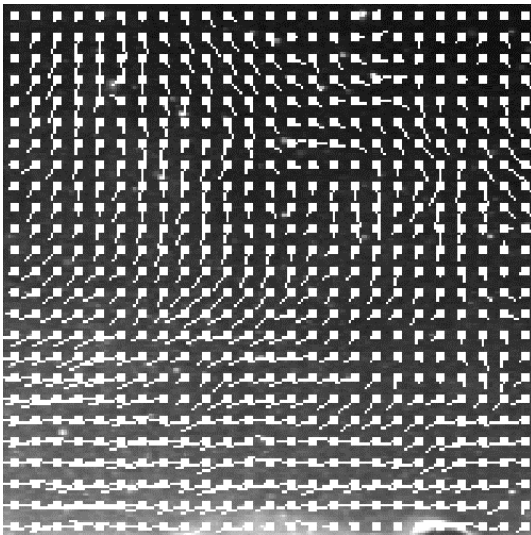*Figure 9.20c Maximum upstream velocity, t = 0.42s*

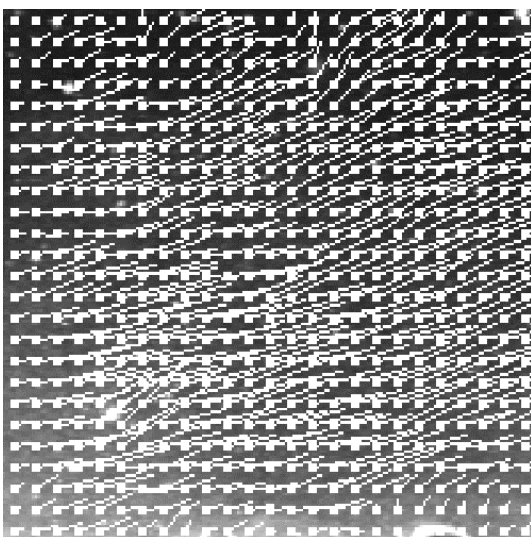*Figure 9.20d Minimum streamwise velocity, t = 1.12s*

Figure 9.20e Maximum downstream velocity, t = 2.2s

The 2D flow fields shown in the images have been obtained using a robust Optical Flow Technique developed in /Garbe 2001/. These flow fields are the 2D projection of the real 3D flow fields on the image plane of the camera. Information from such 2D flow fields is used as input for the 3D reconstruction. In Figure 9.20, one period of the orbital motion above the gravel bed, which is induced by the surface wave, can be identified. During such a period, the velocity vectors are rotating counter-clockwise.

9.4.2   Sand Movement

The analysis of the sediment motion has been carried out using the following two-step approach. First, a motion detection algorithm /Haussecker and Jähne 1993/ is applied to the image sequences acquired by the rigid endoscopes. The result of this algorithm is a binary mask for every image of a sequence. In this mask, a pixel has a value of 1 if motion has been detected at this pixel, and a value of 0 otherwise. Thus, regions which are in motion can be identified using these binary masks. In the second step, we apply an Optical Flow Technique /Jähne et al. 1998; Spies et al. 1999/ to quantify the 2D velocities in the motion regions.
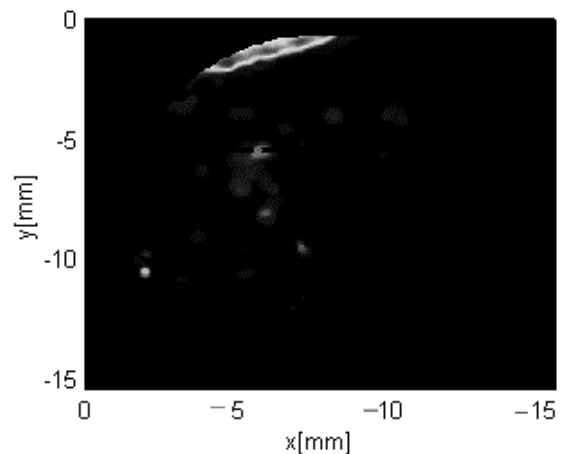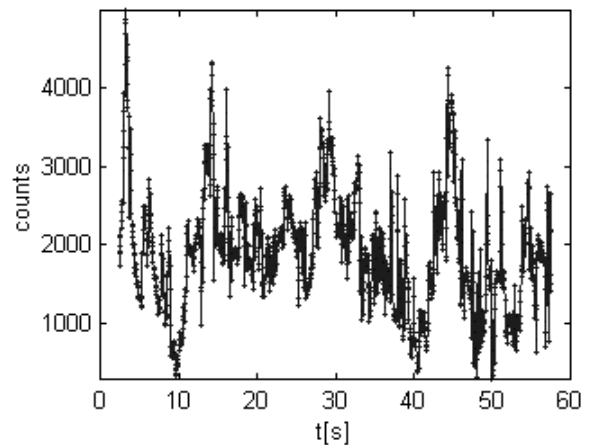

Figure 9.21   Exemplary results of sand motion detection. For a discussion, see text.

Figure 9.21 shows some exemplary results of the (sand) motion detection. These results and the flow fields of Figure 9.20 have been obtained in the same experiment. The upper plot in Figure 9.21 shows a time series of the motion frequency. The ordinate simply gives the number of pixels which are in motion. One sand grain has an area of about 20-200 pixels. We hypothesize, that the detected movement belongs mainly to sand grains. Thus, we can see in this experiment that single moving sand grains have been detected over the complete sequence duration of 60 s. The lower plot in Figure 9.21 shows the spatial distribution of the moving grains. This plot can be considered as a motion map. The black area corresponds to the image size, the endoscope's field of view is a circle inscribed in the black area. The mean flow is from right to left. The motion frequency is encoded in the brightness of the pixels: black corresponds to stationary pixels, white corresponds to the maximum motion frequency. The maximum occurs within an elongated area at the top of the image. This area is located at the interface between sand and gravel. The corresponding image sequence shows the entrainment of sand grains by the orbital motion in the pore flow, which is induced by the artificial generated long waves.

These results for the measured sand movement have to be reviewed in a critical manner. Due to the measuring technique the observed sand grains are lying at the smooth glass window of the endoscope housing (see Figure 9.7). To protect the endoscope the sand was inserted with a rather loose density. Thus, these boundaries do not conform exactly with an interlocked granular structure. A transferability to natural conditions seems to be problematic and has to be proofed more intensive.

The entrainment by the wave motion is shown in more detail in Figure 9.22. In this diagram, a section of the time series of the mean sand grain velocities is shown. The velocities have been obtained by the Optical Flow Technique mentioned above, the (spatial) averaging has been carried out over the regions where motion has been detected. Figure 9.22 shows a repeating pattern of high velocities, with a period of T_W = ~2,0 s, corresponding to the period of the surface waves. The mean velocity has alternating directions: periods of high streamwise (positive u) and low vertical (negative v) are followed by periods of low streamwise (negative u) and high vertical (positive v) velocity. In Figure 9.21 we see that the boundary of the sand layer (corresponding to the bright area) is inclined downwards in flow direction, which explains the directions of the mean velocities in Figure 9.22: sand grains are swept along the inclined boundary.
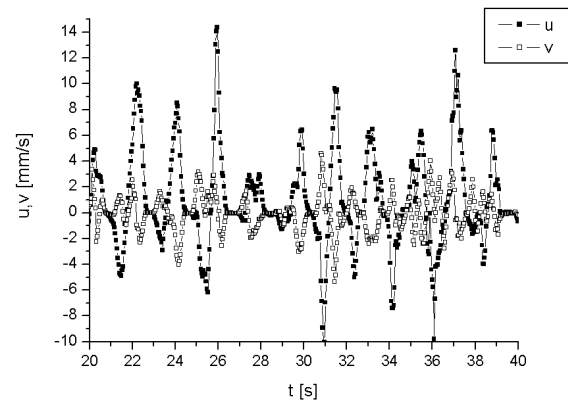

Figure 9.22 *Mean velocity of moving sand grains entrained by the wave motion. For a discussion, see text*
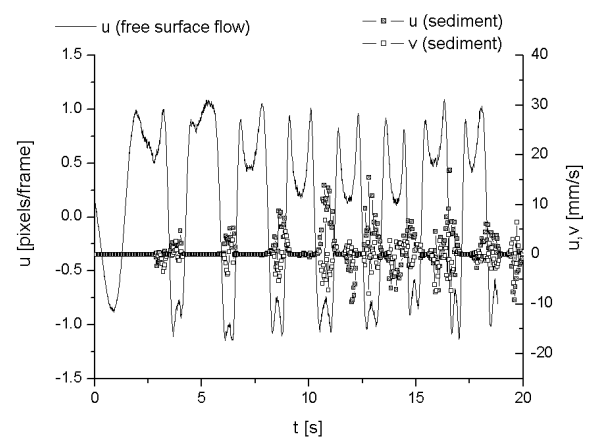

Figure 9.23 *Correlation of mean velocity of entrained sand grains and mean streamwise velocity of the free surface flow. The peaks of the sand motion appear shortly after the streamwise velocity peaks, because the endoscope observing the sand motion is located 50 cm downstream of the free surface flow measurement area.*

Finally, Figure 9.23 shows the correlation of the mean velocity of the entrained sand grains and the mean streamwise velocity of the free surface flow. The mean free surface flow velocity has been obtained by spatial averaging of all velocity vectors in one image (like the ones shown in Figure 9.20). The free surface flow velocity is given by the left ordinate, in units of pixels per frame. The right ordinate shows the mean velocity of the sand grains. As we can see in Figure 9.23, the entrainment of sand grains takes place right after the free surface flow velocity reaches its maximum (in downstream direction). This is consistent with the streamwise location of the measurement areas: the sand motion is measured about 50 cm downstream of the free surface flow measurement.

9.4.3 Micro Pressure Sensors (MPS)

The analysis of the pressure signal gained by the MPS is less difficult than the Optical Flow Technique. Figure 9.24 presents the measured dependency of rms(p) with increasing shear stress τ_0. Both values are non-dimensionalysed by the critical shear stress τ_{0c}, defined by /Shields 1936/. At τ_0/τ_{0c} = 0.6 low mobility conditions were detected as single stones passed the measuring area. This value conforms to the initial point of motion defined by /Wilcock 1996/ at Fr_{c*} = 0.035. In order to mechnical deformation of the whole sensible measuring system larger values of τ_{0c} = 8.8 N/m² were not examined.

All curves in Figure 9.24 increase linear with the instability criteria. Focusing on the two sensors at the interface between gravel and open channel flow at y/d_{mD} = 0.0 (x, +) the inclination can be calculated to a ratio of rms(p)/τ_0 = 3.5 (3.0), see equation 9-1.

Furthermore, the damping of the gravel becomes obvious. Whereas the ratio rms(p)/τ_0 at y/d_{mD} = 1.0 above the gravel can be calculated to C = 10, the ratio is about C = 2.2 at y/d_{mD} = -1.0. Deeper in the gravel bed no difference between vertical positions can be de-tected. The ratio rms(p)/τ_0 is given mostly by C = 1.8.
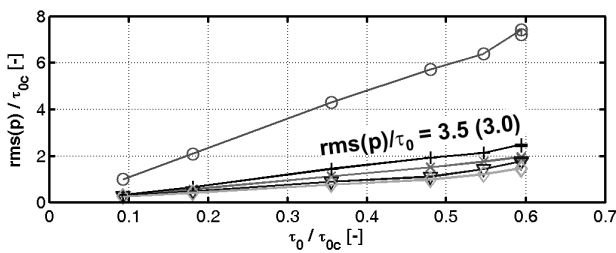

Figure 9.24   rms(p)/τ_0 [-] for increasing instability τ_0/τ_{0c}, τ_{0c} = 8.8 Pa, H_A/d_{mD} = ~20, H_P/d_{mD} = ~10, vertical positions y/d_{mD} [-]: 1.0 (o), 0.0 (x, +), -1.0 (∇), -2.0 ($\diamond$)
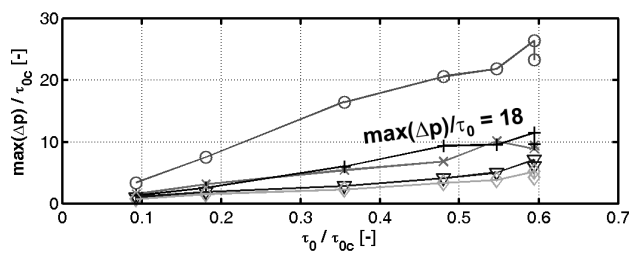

Figure 9.25   max(Δp)/τ_0 [-] for increasing instability τ_0/τ_{0c}, same flow and boundary conditions as in Figure 9.24

Figure 9.25 shows the maximal pressure fluctuations of the pressure signal max(Δp) as a function of shear stress τ_0, both non-dimensionalysed by τ_{0c}. The flow conditions are the same as in Figure 9.24. At y/d_{mD} = 0.0 at the top of the gravel layer max(Δp)/τ_{0c}

leads to a ratio of rms(Δp) = 18 τ_0, which confirms the results of /Emmerling 1973/. As Figure 9.24 and 9.25 resemble each other, the dependence of max(Δp) and rms(p) must be linear.

In order to examine the damping effect of the gravel layer in Figure 9.26 the turbulent kinetic energy (TKE) of the free surface flow is compared to the pressure fluctuations rms(p) directly above and within the gravel layer. TKE and rms(p) are non-dimensionsalysed by u_*^2 and τ_0, respectively.
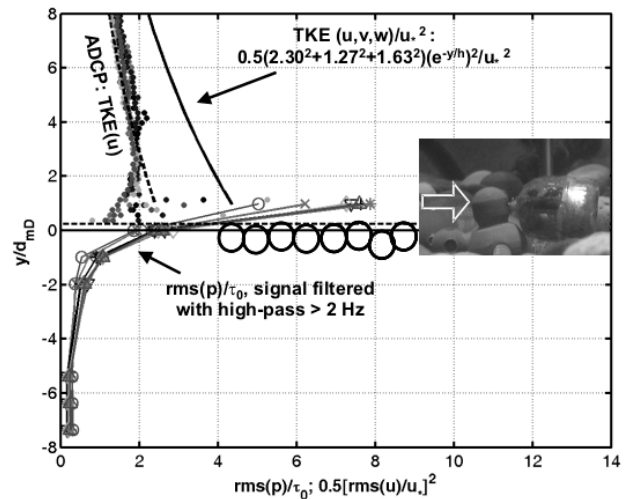

Figure 9.26   Turbulent kinetic energy TKE/u_*^2 [-] in comparison to rms(p)/τ_0 [-]. TKE(u)/u_*^2 (--), TKE(u,v,w)/u_*^2 (-). Increasing instability τ_0/τ_{0c} [-]: 0.09 (O), 0.18 (X), 0.35-0.59 (other symbols), same flow and boundary conditions as in Figure 9.24

The TKE of the velocity fluctuations u' in streamwise direction measured by ADCP conforms with the exponential law known by /Nezu and Nakagawa 1993/:

$$rms(u)/u_* = 2,30\,e^{-y/h} \qquad (9-2)$$

Therefore, the TKE (u,v,w) is supposed to be (see as well /Nezu and Nakagawa 1993/):

$$
\begin{aligned}
TKE&(u,v,w)\\
&= 0.5(2,30^2 + 1.27^2 + 1.63^2)(e^{-y/h})^2\\
&= 4,78\,e^{-2y/h}
\end{aligned}
$$

$$(9-3)$$

Equation 9-2 is denoted by a line ('-') in Figure 9.27, equation 9-3 by a dashed line ('--').

Furthermore, to analyse the turbulence, the turbulent part of the pressure signal had to be separated from the oscillating part that is induced by long waves. Thus, the signal was filtered by a high pass filter of f = 2 Hz seemed to by appropriate. An essential and

exponential damping especially between y/d_{mD} = 0.0 to -2.0 within the gravel layer becomes visible. The (high-pass filtered) value of $rms(p)/\tau_0$ = 5.0-7.5 at y/d_{mD} = 1.0 above the gravel layer does not seem to fit with the turbulent energy of the velocity. As it can be seen by the picture inserted in Figure 9.26, this sensor was orientated directly towards the u-component of the flow. Therefore, the measured signal contains both, the TKE(u) and the pressure fluctuations. A simple subtraction of the TKE(u) value gained by the ADCP could reveal the rate of the turbulent pressure fluctuation. Unfortunately the ADCP is not able to get signals at y/d_{mD} = 1.0. The signal is not very reliable directly above the gravel layer. For a more detailed analysis of the turbulent pressure fluctuations above the gravel layer, the results from the 3-D PTV in the free surface flow will have to be taken into consideration as soon as they are on available.
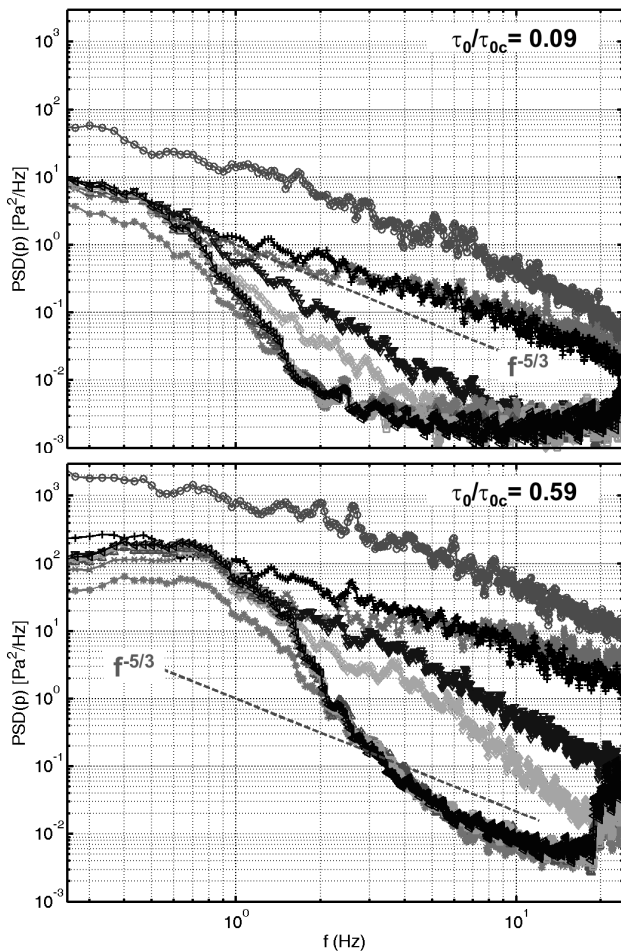
τ_0/τ_{0c} = 0.09 and for an increased instability τ_0/τ_{0c} = 0.59 at low mobility conditions are shown. For the vertical location at y/d_{mD} = 1.0 to 0.0 above and at top of the gravel layer the results agree with Kolmogorov's $k^{-5/3}$ law for the turbulence cascade in open-channel flow /Nezu and Nakagawa 1993/. Within the gravel layer a significant damping between 1 to 3 Hz can be recognized. Below y/d_{mD} = ~-4.0 within the gravel layer there is no significant difference in damping pressure fluctuations higher than 3 Hz. The pressure fluctuations seem to be dominated by the long wave fluctuating water level. For designing a stable filter thinner than H_P/d_{mD} = 4 the influence of turbulence of open channel flow has to be taken into consideration.

Within a coarse estimation, the only difference between the two PSD spectra is the arised power for the increased instability.

Figure 9.27   Power spectral density [Pa²/Hz] for instability τ_0/τ_{0c} = 0.09 and 0.59 (low mobility conditions), τ_{0c} = 8.8 Pa, H_A/d_{mD} = ~20, H_P/d_{mD} = ~10, vertical positions y/d_{mD} [-]: 1.0 (o), 0.0 (x, +), -1.0 (∇), -2.0 (◊) and < -4.0 (other symbols)
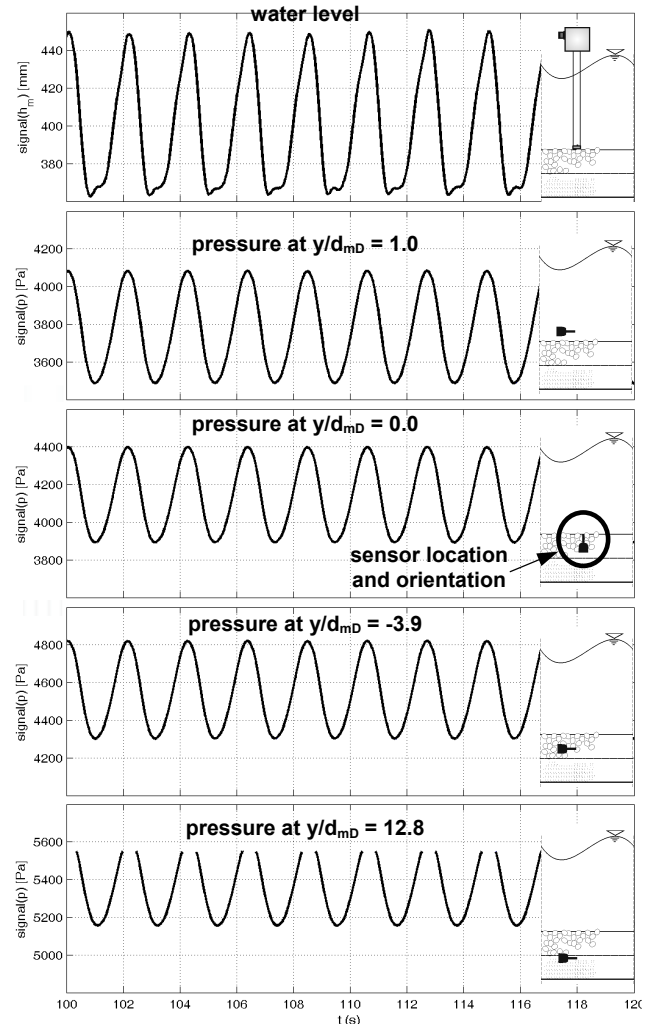

Figure 9.28   Damping of pressure [Pa] above, within and under a gravel filter with H_P/d_{mD} = 10. pressure alteration due to artificially generated waves with H_W = ~88 mm, T_W = ~2.1s. Different scaling at vertical axes.

In Figure 9.27 examples of analysed power spectral densities PSD(p) [Pa²/Hz] for a stable status at

Figure 9.28 depicts the damping of waves of a height of H_W = 88 mm and the period T_W = 2.1s. The medium water depth is h/d_{mD} = 38,4 with a gravel layers thickness of H_P/d_{mD} = 9.8. Within this experiment hydraulic contact between gravel and sand was given. Thus, one pressure sensor was mounted within the sand at y/d_{mD} = -11,8 to gain additionally insight in the interface gravel-sand. Due to the superposition of water depth, installation depth and offset of the sensor the maxima are cut off.

The pressure amplitude is damped over the depth as follows (from top to bottom): Starting with a wave height of H_W = 88 mmWC according to 860 Pa, the oscillation above the gravel at y/d_{mD} = 1.0 is mere Δp = 580 Pa. On 'the way' to the gravel layer at y/d_{mD} = 0.0 the double pressure amplitude reaches Δp = 500 Pa. This value does not change significantly within the gravel layer: at y/d_{mD} = -4.0 the value is unaltered at Δp = 500 Pa. Within the sand layer the value of the pressure oscillation is halved to Δp = 580 Pa according to the wave height.

9.5   Conclusions

9.4.3   Summary

A novel experimental setup enabling a synoptic investigation of the flow and pressure fields within and above a gravel layer has been developed. This setup allows synchronous measurements of pressure and velocity within three artificial pores and in open channel flow. Stereo camera setups are used to measure the flow fields straight above the gravel layer and within three artificial pores in the gravel layer. Optical access to the gravel layer is given by flexible fiber-optic endoscopes. Image processing techniques are applied to extract 2-D and 3-D velocity information from the acquired image sequences (3-D PTV, 2-D Optical Flow). The motion of sand grains at the sand-gravel-boundary can be observed by three additional endoscope setups.

A new method to measure pressure fluctuations in open channel flow both on subsurface and within a gravel layer has proved its functionality. Pressure fluctuations are measured with miniature at high temporal resolution piezoelectric sensors.

First results from an experimental study of the interaction between turbulent open channel flow and the hydrodynamic reaction in porous gravel layer have been shown. Results for the power spectral density of pressure fluctuations in the water column and at top of the gravel layer agree with Kolmogorov's $k^{-5/3}$ law for the turbulence cascade in open-channel flow. Within the gravel layer an essential damping between 1 to 3 Hz can be recognized. Below y/d_{mD} = ~-4.0 within the gravel layer there is no identifiable difference in damping pressure fluctuations higher than 3 Hz. Thus, the pressure fluctuations are dominated by the long wave fluctuating water level. For design criteria for stable filters thinner than four times the gravel diameter the influence of turbulence of open channel flow has to be taken into consideration.

9.4.3   Outlook

Analysis of the 3-D PTV Data:

A huge amount of image data has been acquired during the experimental study at the BAW. The evaluation of this data is still in progress. In addition, a number of improvements of the 3-D PTV algorithm are currently implemented to guarantee an optimal performance of the algorithm on the endoscopic image data. First analyses have shown that very large particle displacements are present in image sequences that have been acquired under flow conditions approaching the critical shear stress or in experiments with large surface waves. Since these flow conditions are of particular interest, a reliable tracking of large displacements is a crucial demand. Currently, a multi-scale approach is implemented to handle the large displacements. Further, a comprehensive accuracy assessment of the algorithm is carried out. After the processing of the image sequences with the improved algorithm, future work will comprise a depiction of velocity statistics and a comparison to the ADCP-data as well as to data found in the literature. Further, evaluation techniques like conditional sampling, analysis of coherent structures/burst events (ejections and sweeps) and space-time correlation of velocity and pressure signals will be applied.

Detailed Analysis of the MPS-Data:

To separate the spectra of quasi-static and dynamic amplitudes, a filter-algorithm for separation of regular long-waves from fluctuations induced by turbulence should be developed. The pressure-signal statistics are to be depicted by pressure probability density functions (PDF). Furthermore, a detailed description of damping within the gravel filter and an evaluation of scale dependency for filter design application will be given.

Synoptic Consideration of Velocity and Pressure

With available data-sets of pressure and velocity fields analysed in detail, a space-time correlation of velocity and pressure signals and an analysis of events (burst and sweep detection) is possible. Thus, a synoptic view of velocity- and pressure fields as well as concluding remarks with respect to gravel bed stability can be given.

9.6   References

Aktiv Sensor GmbH, Berlin

http://www.aktiv-sensor.de

Bonnefille, R. 1963

Essais de synthese des lois de debut d'entrainment des sediments sous l'action d'un courant en regime uniforme. Bulletin du CREC, Nr. 5, Chatou

Detert, M., Jirka, G.H., Jehle, M., Klar M., Jähne, B., Köhler, H.-J., Wenka, T. 2004

Pressure Fluctuations Within Subsurface Gravel Bed Caused by Turbulent Open-Channel Flow, In: Proceedings of River Flow 2004, Greco, Carraveta, Della Morte, Napoli, Balkema Publishers

Dittrich, A., Träbing, K. 1999

Turbulenzbedingte Prozesse kleiner Fließgewässer. In: Wasserwirtschaft, Jg. 89, Heft 6, 306 – 311

Drake, T., Shreve, R., Dietrich, W., Whiting, P., Leopold, L. 1988

Bedload transport of fine gravel observed by motion-picture photography. Journal of Fluid Mechanics, Vol. 192, 193-217

Emmerling, A. 1973

Die momentane Struktur des Wanddruckes einer turbulenten Grenzschichtströmung. In: Mitteilungen aus dem Max-Planck-Institut für Strömungs-forschung. Vol. 56. Göttingen

Garbe, C. S. 2001

Measuring Heat Exchange Processes at the Air-Water Interface from Thermographic Image Sequence Analysis. Ph.D. Thesis, Interdisciplinary Center for Scientific Computing, University of Heidelberg.

Grass, A.J. 1971

Structural features of turbulent flow over smooth an rough boundaries. Journal of Fluid Mechanics, Vol. 50, part 2, 233-255

Gyr, A., Müller, A. 1996

The Role of Coherent Structures in Developing Bedforms during Sediment Transport. In: Coherent Flow Structures in Open Channels, John Wiley and Sons, Chichester, England

Haussecker, H. & Jähne, B. 1993

Ein Mehrgitterverfahren zur Bewegungssegmen-tierung in Bildfolgen. In: Proc. 15. DAGM 1993, 24-31, Springer, Berlin

Jähne, B., Haussecker, H., Scharr, H., Spies, H., Schmundt, D. & Schurr, U. 1998

Study of Dynamical Processes with Tensor-Based Spatiotemporal Image Processing Techniques. In: Proc. ECCV 1998, 322-336, Springer, Heidelberg

Klar, M., Jehle, M., Jähne, B., Detert, M., Jirka, G.H., Köhler, H.-J., Wenka, T. 2004

Simultaneous 3-D PTV and Micro-Pressure Sensor Equipment for Flow Analysis in a Subsurface Gravel Layer, In: Proceedings of River Flow 2004, Greco, Carraveta, Della Morte, Napoli, Balkema Publishers

Kline, S.J., Reynolds, W.C., Schraub, F.A., Rundstadler, P.W. 1967

The structure of turbulent boundary layers. Journal of Fluid Mechanics, Vol. 30, part 4, 741-773

Nezu, I., Nakagawa, H. 1993

Turbulence in Open-channel Flows, IAHR/AIRH Monograph Series, Rotterdam, Balkema Publishers

Meyer-Peter, E., Müller, R. 1949

Eine Formel zur Berechnung des Geschiebetriebs, Versuchsanstalt für Wasser- und Erdbau, Nr. 16, ETH Zürich, 1949

Shields, A. 1936

Anwendungen der Ähnlichkeitsmechanik und der Turbulenzforschung auf die Geschiebebewegung. Mitteilungen der Preußischen Versuchsanstalt für Wasserbau und Schiffsbau, Berlin, Heft 26

Spies, H., Beringer, O., Gröning, H. & Haussecker, H. 1999

Analyzing Particle Movements at Soil Interfaces. In: Jähne, B., Haussecker, H. and Geissler, P. (eds.), Handbook on Computer Vision and Applications, Vol.3, 699-718, Academic Press

Raudkivi, A.J. 1982

Grundlagen des Sedimenttransports, Springer-Verlag, Berlin

Wilcock. P.R. 1993

Critical shear stress of natural sediments. Journal of Hydraulic Engineering. Vol. 119, Nr. 4, 491-505

Zanke, U.C.E. 2001

Zum Einfluß der Turbulenz auf den Beginn der Sedimentbewegung. Mitteilungen des Instituts für Wasserbau und Wasserwirtschaft, Universität Darmstadt, Heft 120